Dynamic Load on Interphase Spacers Due to Ice Shedding

Abdelrahman Moawad[1], László E. Kollár[1], Alajos Bognár[2]

[1] *Savaria Institute of Technology, Eötvös Loránd University, Budapest, Hungary*
[2] *FCI Composite Insulator Ltd, Tápiószecső, Hungary*

abdomoawad@student.elte.hu, kl@inf.elte.hu, bognar@fcicomposite.hu

Abstract— **The main goal of this project is to study the vibration of conductors with interphase spacers (IPSs), which is produced under the effect of ice-shedding. The axial loads on the spacers are determined during the vibration followed by the sleet-jump, then the buckling behavior of the IPS is examined in a separate model. The results concerning the axial loads on the IPS are obtained by applying three approaches. The first approach means the experimental study, which involves material tests and a buckling test on samples of fiber-reinforced plastic (FRP) material that is used in manufacturing the IPSs. The second and third approaches are applied simultaneously, and they include analytical modeling and numerical simulations. The analytical model is implemented in MATLAB, and it will be used in building and verifying the numerical model. This numerical model is created using the ANSYS Workbench software, and it is used to simulate ice-shedding from two conductors that are separated by two IPSs.**

Keywords— ***buckling, ice shedding, interphase spacer, material test, modeling, vibration***

I. Introduction

Transmission line conductors are now common in everyday life, as they mean the main method to transmit electricity over long distances, also they exist in every country all around the world. Electricity can indeed be transmitted through underground cables, but in this case, the cost will be 7-10 times higher [1]. Transmission lines are exposed to natural phenomena, which lead to different kinds of vibration. Those phenomena include the wind, ice shedding [2], or the impact of any object. Wind-induced vibration may be divided into three categories. Aeolian vibration is a high-frequency, low-amplitude vibration, galloping is a high-amplitude, low-frequency vibration, while the wake-induced oscillation typically occurs in conductor bundles and is characterized by frequency and amplitude in between those in the previous two categories.

Line compaction is based on decreasing the interphase spacing. This results in a greater risk of interphase flashover when two conductors approach each other. High-amplitude conductor vibration may be induced by wind or ice shedding. When wind acts on a conductor that has an asymmetrical cross-section, e.g. due to ice accretion, then galloping develops. Shedding of ice may have similar consequences to galloping as it leads to high-amplitude vibration that causes failure of transmission line elements. The ice or snow that is deposited on the conductor will lead to an increase in the conductor sag and the strain energy stored in the conductor. When this load drops from the conductor, the strain energy will be converted into kinetic energy and then potential energy until it reaches its maximum height. This phenomenon is called 'sleet jumping.' The amplitude of the jump can be higher than the clearance allowance between the two phases, which will cause a flashover. Moreover, the conductor forms a new static equilibrium after the ice shedding with smaller sag, and if ice from the upper conductor is still not shed, it might cause an air gap reduction between the phases causing a short circuit.

Methods have been developed to prevent flashover including the introduction of IPSs between the phases. Properly chosen IPSs may provide a solution since the vibration amplitude can be reduced to a small enough level that ensures the line security. The IPS occurs as additional weight in the transmission line; therefore, the classical porcelain insulators could not be widely applied due to their high mass/strength ratio. The FRP composites have a significantly more advantageous mass/strength ratio; consequently, their application is widespread including ultra-high-voltage-alternating-current transmission lines even at sections across valleys and rivers.

Research to simulate the ice-shedding phenomenon has been carried out for decades both experimentally [3] and numerically [4]. More recently, References [5, 6] studied the vertical vibration and rotation of bundled conductors following sudden ice shedding and ice shedding propagation. Reference [7] introduced a method to determine the height of the sleet jump of a conductor after ice shedding. This method is based on the geometrical relation of each of the spans, stress-sag relation, energy conservation, and dynamic relation of the suspension insulators of a multi-span transmission line following ice shedding. Further literature discussed the prevention of conductor ice-shedding by IPS [8], and the modern structure of the IPS was introduced in [9].

The composite insulators are slender structures where buckling determines the limitation of application. Buckling results in plastic deformation for the materials used formerly; however, the FRP core of composite insulators remains elastic for a limited time interval during buckling. This paper aims to study the process of buckling together with the developing load and stress in FRP composite insulators during buckling that occurs due to the vibration of phases following ice shedding.

II. Theoretical Background

The towers are designed to support the weight of the conductors with a specified sag. The required pre-tension force is obtained based on the catenary profile that the suspended conductor forms. If the ratio between the sag and the span length is small enough (i.e. less than 1:8), the conductor profile can be closely approximated by a parabola [10, 11].

Equation 1 and Equation 2 determine the tensile force F_h and F_H, required to suspend the conductor under its weight with sag h, assuming parabolic profile and catenary profile, respectively. The difference between the results is in the range of 0.1 % if the small-sag assumption is satisfied. The w_0 denotes weight per unit length of the cable.

$$F_h = {w_0 \cdot L^2}/{8 \cdot h}, \quad (1)$$

$$h = \frac{F_H}{w_0} \cdot \left(\cosh\left({w_0 \cdot L}/{2 \cdot F_H}\right) - 1\right), \quad (2)$$

$$S = \frac{2 \cdot F_H}{w_0} \cdot sinh\left(\frac{w_0 \cdot L}{2 \cdot F_H}\right), \quad (3)$$

$$\varepsilon = \frac{\sigma}{E} = \frac{F_H}{E \cdot A_C} \quad (4)$$

Equation 3 provides the total length of the suspended conductor forming the required sag. This length is obtained for the static equilibrium of the system after applying the pretension force. This tensile force will indeed cause elongation in the cable, and this elongation can be represented by defining a pre-strain in the conductor. This pre-strain can be calculated by Equation 4 based on Hook's law.

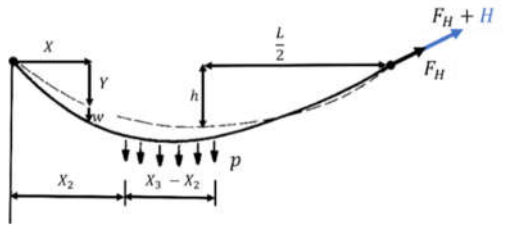

Fig. 1: Uniformly distributed load on a conductor.

Ice occurs as a distributed load on the conductor as Fig. 1 shows. If ice load is assumed on the entire length of the conductor then $x_2 = 0$ and $x_3 = L$, and the following equations determine the increment in horizontal conductor tension H and the vertical displacement w due to the distributed load [12],

$$\boldsymbol{H^3} + \left(2 + \frac{\lambda^2}{24}\right)\boldsymbol{H^2} + \left(1 + \frac{\lambda^2}{12}\right)\boldsymbol{H} - \left(1 + \frac{\boldsymbol{P}}{2}\right)\frac{\lambda^2}{12}\boldsymbol{P} = 0, \quad (5)$$

$$\boldsymbol{w} = \frac{1}{2(1+\boldsymbol{H})} \cdot \left(1 - \frac{\boldsymbol{H}}{\boldsymbol{P}}\right) \cdot \boldsymbol{x} \cdot (\boldsymbol{1} - \boldsymbol{x}), \quad (6)$$

where $\boldsymbol{H} = \frac{H}{F_H}$, $\boldsymbol{P} = \frac{\boldsymbol{p}}{w_0}$, $\boldsymbol{w} = \frac{w}{{PL^2}/{F_H}}$, $\boldsymbol{x} = \frac{X}{L}$ and λ is a parameter calculated from the geometrical and material properties of the suspended conductor.

Conductors may vibrate due to several reasons, and first, the different modes of vibrations should be introduced. The natural circular frequencies of the conductor are based on the structure and the material of the conductor, and those frequencies can be calculated after solving the equations of motion [11]. Natural circular frequencies can be determined for motions in two planes, in the transverse horizontal motion and in the in-plane motion, which is divided into antisymmetric and symmetric modes.

In transverse horizontal motion, there is no additional cable tension induced by the motion. This is consistent with experience since, for a hanging chain, the first swinging mode is the easiest to be excited. Therefore, if the disturbance has no in-plane component, it will cause only transverse horizontal motion. The natural frequencies can be obtained using the following equation [11]:

$$f_{trans.n} = \frac{n}{2 \cdot L} \cdot \sqrt{\frac{F_H}{m}}, \; n = 1,2,3, \ldots \quad (7)$$

The in-plane motion has two forms, involving either antisymmetric vertical and symmetric longitudinal components, which is called antisymmetric in-plane motion, or the opposite, symmetric vertical, and antisymmetric longitudinal components, which is called symmetric in-plane motion. The natural frequencies are calculated from Equations 8 and 9 in which β is obtained as the solution of a transcendental equation [11].

$$f_{antis.n} = \frac{n}{L} \cdot \sqrt{\frac{F_H}{m}}, \; n = 1,2,3, \ldots \quad (8)$$

$$f_{symm.n} = \frac{\beta}{2 \cdot \pi} \cdot \sqrt{\frac{F_H}{m}}, \quad (9)$$

The structural damping of the conductor contributes to vibration attenuation. This damping is considered Rayleigh damping, where the damping matrix $\boldsymbol{C}$ is proportional to the mass matrix $\boldsymbol{M}$ and the stiffness matrix $\boldsymbol{K}$, and two constants, α_{mass} and β_{Stiff} must be defined.

$$\boldsymbol{C} = \alpha_{mass}\boldsymbol{M} + \beta_{Stiff}\boldsymbol{K} \quad (10)$$

The two constants can be obtained from Equations 11, 12 [13]:

$$\alpha_{mass} = 2\omega_1 \cdot \xi_1 - \beta_{stiff} \cdot \omega_1^2, \quad (11)$$

$$\beta_{Stiff} = 2 \cdot \frac{\left(\omega_2 \cdot \xi_2 - \omega_1 \cdot \xi_1\right)}{\omega_2^2 - \omega_1^2}, \quad (12)$$

To calculate the two coefficients, two natural circular frequencies, ω_1 and ω_2, are needed. They can be obtained from two vibration modes: the first mode of the symmetric and the first mode of the antisymmetric in-plane motions. Those analytical results were derived based on a free single conductor, and consequently, the modal analysis will also be applied to a single conductor in the numerical model by applying the Modal analysis system in Ansys. Numerical results will be compared with the analytical calculations, then the modal analysis of the full structure can be carried out.

Apart from natural circular frequencies, Equations 11 and 12 require two damping ratios, ξ_1 and ξ_2. The relative damping ratio is assumed to be 2 % for bare conductors and 10 % for iced conductors [14]. In the present study, the damping ratio of 5 % is applied, i.e., $\xi_1 = \xi_2 = 0.05$.

During high-amplitude vibrations, remarkably high axial loads arise in the IPS, which may lead to buckling, and for that reason, the IPS needs to be designed very carefully considering the high axial loads. This design is based on the structure that also determines how many IPSs are used in a span with a specific length. Equation 13 is used to define the minimum load that is required for buckling. This load determines the design of the spacers, and it is known as Euler's load for buckling:

$$P_{Euler} = \frac{\pi^2 \cdot E \cdot I}{l_0^2} \rightarrow \sigma_{cr} = \frac{\pi^2 \cdot E \cdot I}{A \cdot l_0^2}, \quad (13)$$

where E is Young's modulus, I is the minimum moment of inertia, l_0 is the effective length of the rod that depends on the end condition of the member and can be defined based on reference [15]; while A represents its cross-sectional area. The Euler's angle that is the angle of the buckling rod at the pinned end is determined from the equality of the Euler stress and the bending stress [16].

After introducing the theoretical background and defining the required equations a MATLAB application was developed to carry out the analytical calculations described in this section.

III. Material tests

The traditional IPS is made of porcelain which is characterized by low breaking strain what leads to a catastrophic failure as soon as the compression force exceeds the Euler's load. The modern IPSs are made of composite materials that can withstand loads higher than the Euler's load for buckling, and still, they do not break. They can do that because they have high breaking strain energy due to the FRP.

Zwick / Roell testing machine was used to perform a 3-point bending test as shown in Fig. 2. During the tests, the predefined load position was 40 mm apart from each support unit, and a pre-load of 10 N is applied with a speed of 3 mm/min followed by a test speed of 2 mm/min. The tests were conducted on samples made of the specific composite FRP. In total, eight tests were performed on samples with two different diameters: four tests on samples with a diameter $d = 8$ mm, whereas further four tests on samples with a diameter $d = 6$ mm.

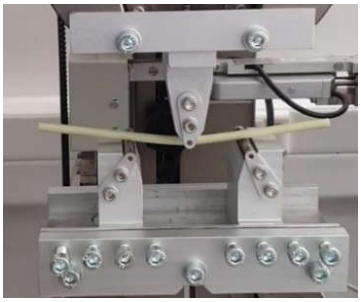

Fig. 2 Tested sample made of the FRP material.

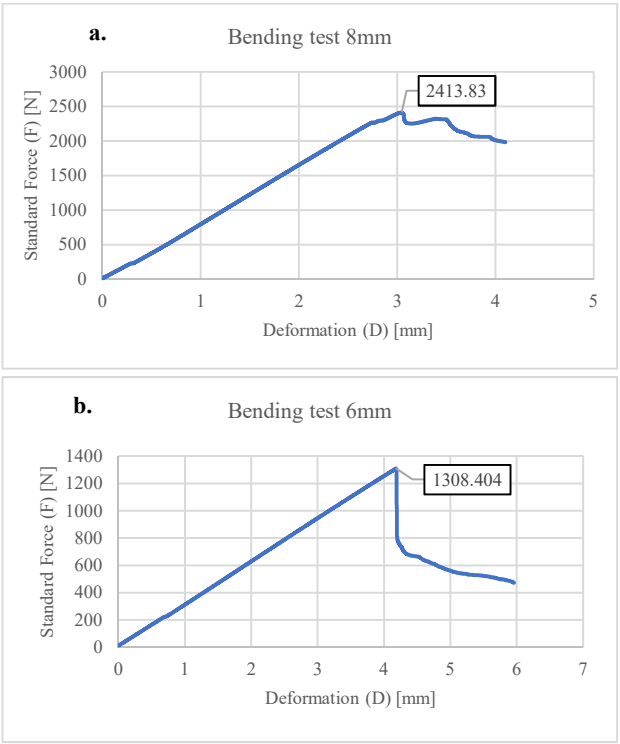

Fig. 3 Two examples of the bending tests with samples of different diameters (a) $d = 8$ mm; (b) $d = 6$ mm

Fig. 3 presents the force-deformation graphs. First, the standard force applied to the specimen increases, and so does the corresponding deformation. The deformation is elastic at the beginning, which means that if the test is interrupted at that time instance, the material will gain back its original shape. After the yield point, the deformation becomes plastic at which the material will be permanently deformed. This force was measured and then used to find the flexural strength σ_{fs} and the modulus of elasticity E_f after applying the following equations:

$$\sigma_{max} = \sigma_{fs} = \frac{M_{max}}{K}, \quad (14)$$

where $M_{max} = \frac{F_{max} \cdot L}{4}$, and $K = \frac{\pi \cdot d^3}{32}$

$$E_f = \frac{m \cdot L^3}{12\pi \cdot R^4}, \quad (15)$$

in which F_{max} is the maximum force, L is the length between the two supports, m is the slope of the graph of the force over the deformation, defined as $m = \frac{F}{D}$ (of the elastic region), and d and R are the diameter and radius of the sample, respectively.

The average values obtained for the flexural strength and modulus of elasticity from the measurements were introduced in the numerical model.

IV. Numerical simulation of vibration of conductors with IPSs

A. *Problem definition and aim of the analysis*

The aim of the numerical study is to simulate the high-amplitude vibration following ice shedding from a conductor and then to examine its effects on the IPS with particular attention to buckling.

Numerical models were constructed using the finite element commercial software ANSYS. A line-body model is built in the Transient Structural analysis system to represent the transmission line. The exact geometry can be verified analytically using Equations 1-4, and the natural frequencies can be evaluated by Equations 7-9. Ice load and ice shedding are simulated by applying a distributed load on the conductors in the line-body model and removing it at a specific time instance. The load removal causes the system to vibrate with high amplitude, which simulates the sleet-jump phenomenon. The axial loads acting on the IPS can be obtained, and their effects are studied in a 3D sub-model of the IPS.

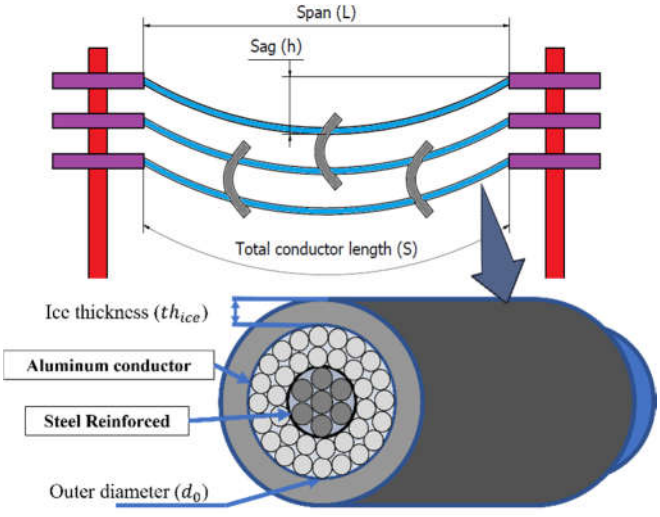

Fig. 4: Suspended conductors with IPS

Fig. 4 represents the full structure of a transmission line. The lower two conductors with two IPSs are considered in the numerical model since the shedding of the lowest one when the upper one is still loaded has the highest possibility to lead to flashover.

In this model aluminum conductor steel reinforced (ACSR) is considered, whose data were received from a line operator. The two conductors are separated by two IPSs made of FRP material. The material and the geometry data of the conductors are listed in Table 1. The geometry of IPSs is given in Fig. 4, and three different diameters were considered in the simulations, which are denoted by d_{IPS}, $0.83\,d_{IPS}$ and $0.57\,d_{IPS}$. The material properties were obtained from measurements as explained in Section III.

TABLE 1: GEOMETRICAL AND MATERIAL DATA OF THE CONDUCTOR

Property		Unit	Value
Span length	(L)	[m]	400
Sag	(h)	[m]	11.09
Mass per unit length	(m_0)	[kg/m]	1.457
Conductor diameter	(d_o)	[mm]	27.72
Effective area	(A_c)	[mm^2]	454.5
Young's modulus	(E)	[GPa]	65.727
Poisson's ratio	(ν)	[1]	0.33

B. Description of the geometrical models

1) Line body geometry: The geometry in the line-body model consists of two conductors with two IPSs as shown by the bottom two conductors in Fig. 4. The total final length of the conductors is calculated based on Equation 3. This final length is obtained after the conductor was elongated due to the tensile force that holds the conductor in the suspended position. The initial strain and the force are obtained from Equations 4 and 1, respectively. Thus, it was calculated that the tensile force required to hang each cable is $F_H \approx 27900\ N$, the total length $S = 400.82\ m$ and the pre-strain $\varepsilon = 0.000919$.

2) Geometry of the 3D sub-model of IPS: The IPS is made of a special fiber-reinforced matrix, and it is assumed to have a simple circular cross-section. As the IPS will be connected to both conductors, it consists of two connection points that the conductors will go through. In the 3D structure, the total length of the IPS is a bit longer than in the line-body model in order to have extra material that supports those connection points.

This geometry will be considered only in the case of the sub-modeling where the buckling behavior of the IPS is studied, whereas in the line-body model that simulates the vibration of the entire system following ice shedding, the IPS is considered as a simple cylinder with a length that is equal to the distance between the two phases.

C. Description of Mesh

1) Line-body model: It was examined that changing the mesh size above 45 elements in a conductor did not have any significant effect on the final static equilibrium position of the system. Therefore, a mesh was created with a total of 135 nodes and 45 elements.

2) Sub-model for the IPS: Results with higher precision are required for the IPS since the stress regions are studied. For this reason, a finer mesh is applied to the 3D geometry of the IPS in a separate sub-model. This mesh would be in a quadratic order with a total nodes of 28670 and with 14988 elements.

D. Loads and boundary conditions

Loads and constraints have to be defined so that they can adequately describe ice shedding and the subsequent sleet-jump phenomenon. First, the ice load should be determined, then both kinematic and dynamic boundary conditions have to be applied, and finally, boundary conditions in the sub-model for IPS are defined for studying the buckling behavior.

1) Self-weight of conductor and ice load: The bare conductor without any extra load on it is subjected to its weight that acts as a load and that affects the supports as well. The conductor is strained due to pretension, which can be considered by applying a pre-strain command in the numerical model for the desired geometries, i.e. for the conductors. The ice is gradually formed on both conductors adding external loads on them that also increase the force acting on the supports. The ice load is considered a distributed load, and it is calculated from Equations 16-18 after ice thickness and density are given as follows: $th_{ice} = 18\,mm$, and $\rho_{Ice} = 735\ {}^{kg}/_{m^3}$.

$$A_{ice} = \left((d + 2 \cdot th_{ice})^2 - d^2\right) \cdot \frac{\pi}{4} \cdot 10^{-6}\ \mathrm{m}^2 \quad (16)$$

$$m_{o_{ice}} = A_{ice} \cdot \rho_{ice} = 1.9\ {}^{kg}/_{\mathrm{m}} \quad (17)$$

$$F = m_{o_{ice}} \cdot L \cdot g \approx 7450\ \mathrm{N} \quad (18)$$

Two ice shedding scenarios will be simulated. Both conductors are loaded with ice in the first one, and ice sheds from the lower one, while the upper one is still loaded. Then, ice also sheds from the upper conductor due to the vibration of the lower conductor. Only the lower conductor is loaded in the second scenario, and the ice sheds from it causing the sleet jump. The steps of both scenarios are the same, and the axial loads will be compared, which arise in the IPS during the vibration caused by the sleet-jump phenomenon.

2) Kinematic boundary conditions: The kinematic boundary conditions are the constraints that ensure the support of the structure. Initially, a line is defined, whose length is equal to the total length of the conductor (S = 400.82 m). Since the suspended conductors are free to rotate about the transverse axis (Z-axis), remote displacements are used where the rotation about the Z-axis is free. The following kinematic boundary conditions are set up to obtain the catenary profile.

A. Moving Upper Support (remote displacement)
   - Move the end of the upper conductor to the span length and fix it
   - Allow only rotation around Z-axis.

B. Moving Lower Support (remote displacement):
   - Move the end of the lower conductor to the span length and fix it
   - Allow only rotation around Z-axis.

C. Standing Upper Support (remote displacement)
   - Fix the left side of the upper conductor and allow only rotation around Z-axis.

D. Standing Lower Support (remote displacement):
   - Fix the left side of the lower conductor and allow only rotation around Z-axis.

E. 2-D displacement:
   - Fix the structure in the XY plane $Z = 0$.

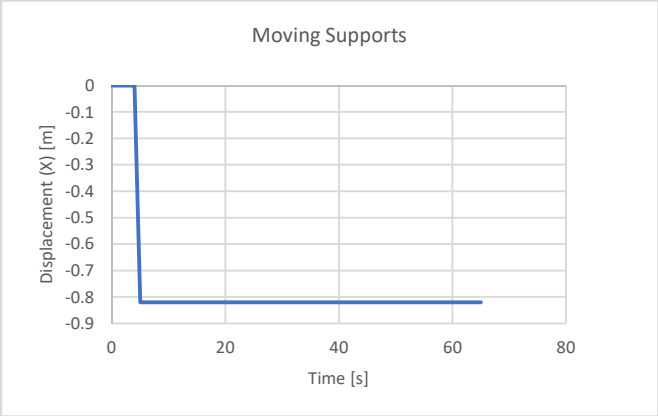

Fig 5: Moving supports in Kinematic boundary conditions

3) Dynamic boundary conditions: The dynamic boundary conditions are introduced to apply the dynamic effects of the environmental changes on the structure. Those dynamic effects are presented in the form of the standard Earth gravity and the load generated due to the ice accretion on the conductor followed by ice shedding leading to sleet jump of the conductors.

F. Lower conductor ice load (Force $F = 7450$ N):
- Apply line load to simulate the ice weight.
- The weight stays for 8 seconds to reach static equilibrium, then it falls.

G. Upper conductor ice load (Force $F = 7450$ N):
- Apply line load to simulate the ice weight.
- The weight stays for 10 seconds to reach static equilibrium, then it falls.

H. Acceleration:
- Applied on the full system to simulate the Earth's gravity $\left[a_y = 9.81\ {}^{m}/_{s^2}\right]$.
- It must be ramped acceleration (increases in 3 s in the numerical model from zero to the defined value)

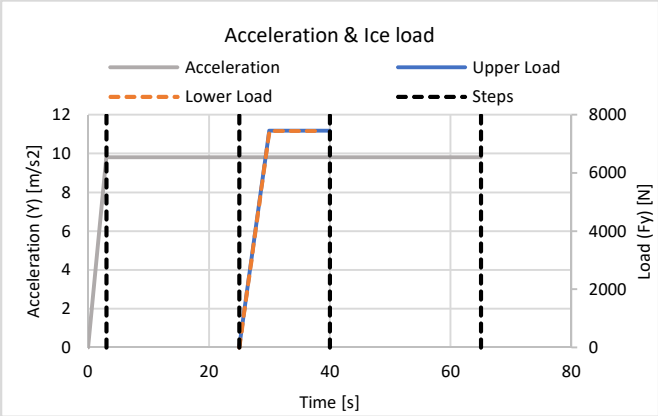

Fig. 6: Dynamic boundary conditions of the line body model

The set-up of boundary conditions is divided into four main steps. Fig 5 and 6 represent the application of boundary conditions of the analysis over time. The first step considers the self-weight of the system, which will cause the moving supports on the right side to move towards the center of the conductors. Then, 20 s pass to allow the system to reach the equilibrium state before the ice load is added to the conductors. Another 18 s pass and the lower cable sheds followed by the shedding of the upper one 2 s later, which causes the vibration of the system.

4) Sub-model of IPS: The geometry of the IPS was drawn in Fig. 4, and the following boundary conditions are applied for studying the buckling behavior (Fig. 7):

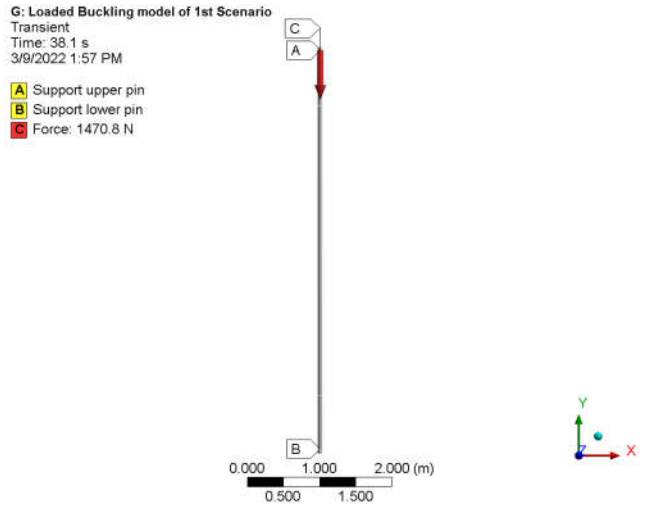

Fig. 7: Boundary conditions of the 3D sub-model

A. Remote displacement in the upper pinhole (Kinematic B.C)
- Allow only vertical displacement [Y-axis]
- Allow only rotation around Z-axis.

B. Remote displacement in the lower pinhole (Kinematic B.C)
- Allow only rotation around Z-axis.

C. Axial force in the upper pinhole (Dynamic B.C.)
- An axial force is introduced in the direction of only the Y-axis with an eccentricity of 4 mm.

V. Results and Discussion

Table 2 reveals that the numerical results obtained from the ANSYS modal analysis of a single conductor show excellent agreement with the analytical results calculated by the MATLAB implementation. This means that the numerical results are reliable.

TABLE 2: COMPARISON BETWEEN THE NUMERICAL AND THE ANALYTICAL RESULTS OF EIGENFREQUENCY

Numerical results using ANSYS Modal		**Analytical results using MATLAB**	
Mode	**Frequency [Hz]**	**Mode**	**Frequency [Hz]**
1	0.16635	$f_{trans.1}$	0.1663
2	0.3327	$f_{antis.1}$	0.3327
3	0.49905	$f_{symm.1}$	0.4990
4	0.66542	$f_{antis.2}$	0.6654
5	0.83182	$f_{symm.2}$	0.8317
6	0.99827	$f_{antis.3}$	0.9981
7	1.1648	$f_{symm.3}$	1.1644

The next step is to obtain the natural frequencies of the full structure. The same geometry and the same material model that is described in Section III were applied. Also, the same kinematic boundary conditions were defined without considering any loads on the structure. The first antisymmetric and symmetric in-plane vibration modes were determined and used to calculate the coefficients of the Rayleigh damping.

In what follows, the loaded structure will be studied. First, the model should be validated, which can be done by comparing the numerical results obtained for deformation and force reaction on supports with and without ice load with those parameters that are calculated based on the theoretical background. Then the numerical model will be used to simulate ice shedding and determine the load on the IPS during such vibration.

1) Model validation: The force reaction on the supports, as well as the vertical deformation of the loaded and unloaded conductor, i.e. the sag of the conductor with and without ice load, are calculated using Equations 1-6 in the MATLAB implementation and compared with the simulation results obtained at two time instances by the ANSYS computation.

The numerical simulation started by applying the weight of conductors, which was considered a dynamic load in the numerical model. This is the reason for the oscillation of the force at the beginning of simulation as shown in Fig. 8.

TABLE 3: ANALYTICAL RESULTS FOR MODEL VALIDATION (TIME MEANS CORRESPONDING TIME INSTANCE IN NUMERICAL SIMULATIONS)

Time [s]	**Force Reaction [N]**	**Vertical deformation (Y-axis) [m]**
$t = 37$ s	$F_H + H \approx 51800$ N	$Y = -13.07$ m
$t = 65$ s	$F_H \approx 27400$ N	$Y = -11.09$ m

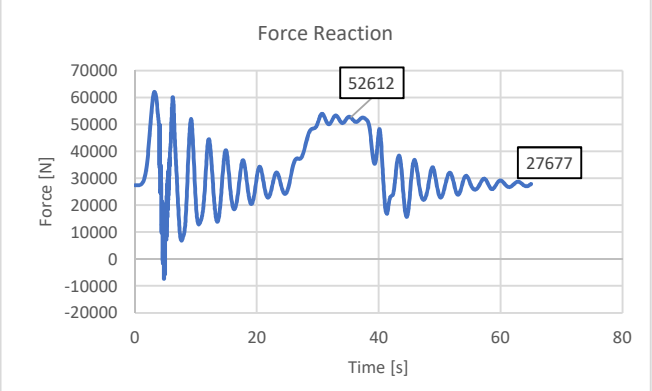

Fig. 8: Force reaction on the right upper support [N] over time [s]

According to Fig. 8, the force reaction in the supports in case of the loaded conductor $F_H + H = 52.6$ kN, which appears at $t = 37$ s, and in case of the unloaded conductor the force reaction reaches $F_H = 27.7$ kN. The comparison with the analytical results listed in Table 3 reveals errors of about 1 %, which is accepted for further analysis.

Fig. 9 shows the vertical displacement of the conductor in the middle of the span as calculated by the numerical model. Comparison with the analytical results presented in Table 3 provides errors in the range of 0.1%, which means that the numerical model is reliable to calculate force and displacement.

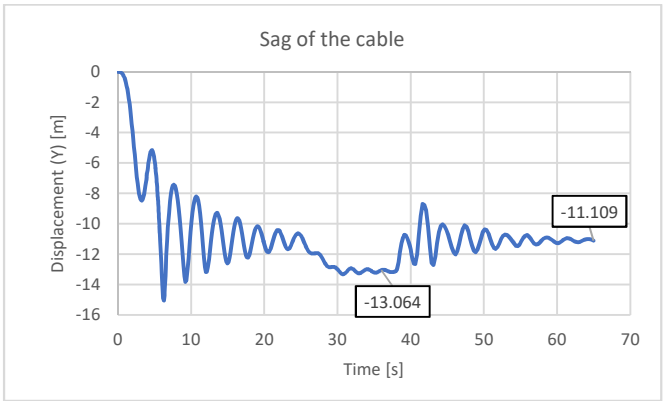

Fig. 9: Change of the vertical displacement [m] over time [s].

2) Loads generated on the IPS: The main aim of the analysis is to obtain the axial load and the deformation of the IPS during vibration following ice shedding. Before analyzing the IPS, a limitation should be set for the maximum allowed stress. The analytical calculations are carried out based on Euler's equation for buckling which is shown in Equation 13. According to the theory, the results for the critical stress of the IPS with the greatest diameter $\sigma_{critical} \approx 4\ MPa$. The allowed stress with a safety factor of $n = 2$ is calculated as $\sigma_{allowed} = \frac{\sigma_{fs}}{n} = 500\ MPa$, which corresponds to a vertical load $P = 13110\ N$ and Euler angle $\alpha_{Euler} = 30°$.

The line-body model is used to simulate the two ice-shedding scenarios described in Section IV, then the highest compression force can be determined and applied in the sub-model of the IPS.

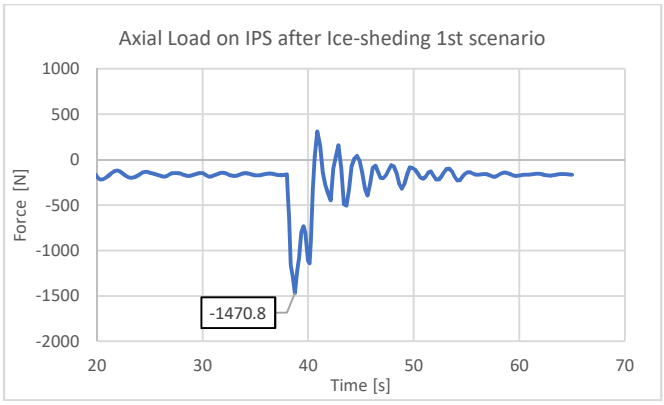

Fig. 10: Axial load [N] on IPS over time [s] in the first scenario

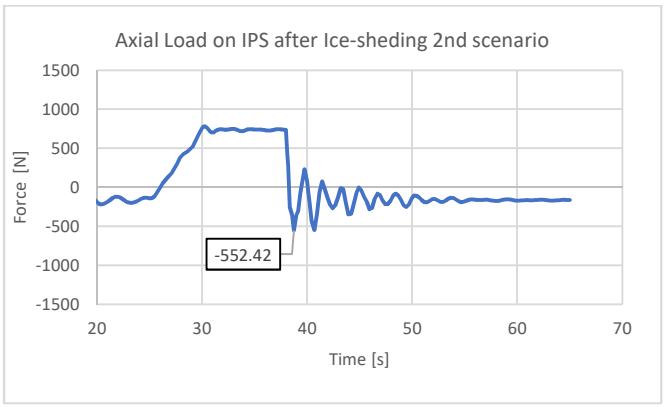

Fig. 11: Axial load [N] on IPS over time [s] in the second scenario

Fig. 10 shows the time history of axial force acting on the IPS during the first shedding scenario. The maximum compression force arises a few seconds after the ice-shedding, and then it decays. Fig. 11 shows that there is a high-tension force before the ice shedding in the second scenario, which corresponds to the ice load only on the lower cable. This state is followed by the greatest compression force when ice sheds from the lower conductor. However, this value is significantly smaller than the maximum compression force obtained in the previous scenario.

Based on the above results, the axial force obtained in the first scenario is applied in the sub-model for the IPS. Before the stress analysis, the buckling behavior is studied in ANSYS by creating an Eigenvalue buckling model based on the 3D geometry of the IPS. This model is based on a static structure with a load of $P = 1$ N applied for just one numerical time unit, and load multipliers are determined, which are required for different modes of buckling. The first mode is of interest as it occurs under the lowest axial load.

Fig. 12 shows the deformed shape of the IPS in the case when it is subjected to axial load $P_{critical_1} = 12609$ x 1 N. This value is very close to that obtained analytically based on Equation 13, which is $P_{Critical} = 12615$ N.

In what follows, the stress analysis is carried out using the maximum axial force obtained in the first shedding scenario and presented in Fig. 10. Meanwhile, the analytical equations built to the MATLAB application are also applied to verify the results.

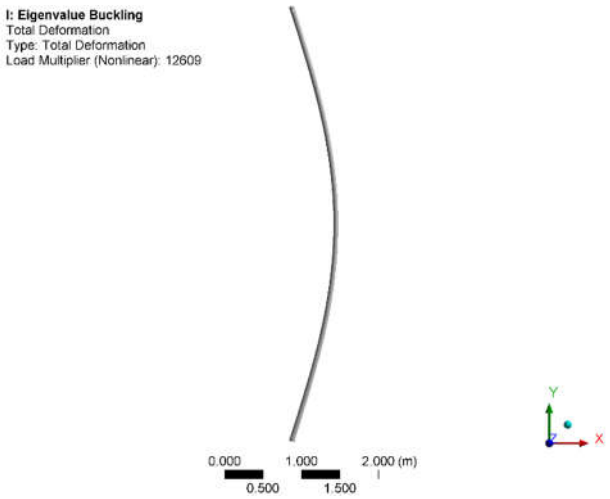

Fig. 12: First buckling mode of load multiplier $n_P = 12609$ times

TABLE 4: ANALYTICAL AND NUMERICAL RESULTS OF THE BUCKLING ANALYSIS OF IPS WITH d_{IPS}

Result	**Axial load** [N]	**Euler load** [N]	**Direct stress** [MPa]	**Critical stress** [MPa]	**Buckling stress** [MPa]
Analytical	1470	12615	0.47	4.05	No buckling
Numerical	1470	12609	0.67	4.05	No buckling

Table 4 reveals that the results of the analytical and the numerical calculations coincide. The direct stress is significantly below the critical stress; therefore, buckling does not occur. It can also be seen that the direct stress is higher in the numerical simulation than in the analytical calculations. This may be due to the dynamic effects of ice shedding, because these effects cannot be represented by the analytical equations, as those equations only describe the static forces.

Since the direct stress is much smaller than the critical stress, other spacers with smaller diameters are also tested, and the smallest spacer that does not suffer buckling under the same load can be chosen as optimum.

TABLE 5: BUCKLING ANALYSIS OF SMALLER IPSS

Results	0.83 d_{IPS}		0.57 d_{IPS}	
	Numeric	Analytic	Numeric	Analytic
Euler's Load [N]	5854.7	5855	1313.1	1345
Critical stress [MPa]	2.76	2.76	1.29	1.321
Axial load [N]	1403	1403	1317	1345.13
Direct stress [MPa]	0.87	0.66	-	1.322
Horizontal deformation [mm]	0.72	0	48.15	45.18
Vertical deformation [mm]	0.08	0	1.7	1.04
Euler angle [°]	$\alpha_{\text{Euler}} \approx 0°$		$\alpha_{\text{Euler}} < 2°$	
Buckling Stress (σ_b) [MPa]	No Buckling	No Buckling	Buckling 18.56	Buckling 14.15

According to the numerical results presented in Table 5, the maximum axial load obtained from the line body model in the case of the smallest diameter ($0.57\ d_{IPS}$) is higher than the critical Euler load that was obtained from the Eigenvalue model. Thus, the load following ice shedding will cause buckling in the spacer, but the Euler angle does not exceed two degrees. The analytical results also confirm that the force is just higher than the Euler load. Even though the spacer undergoes buckling, the stress is much smaller than the flexural strength of the material, which means that the spacer will retain its original shape after the load is removed.

A rule of thumb for the selection of the IPS is represented as $d_{IPS} \geq L_{IPS}/100$. The IPS with a diameter of $0.83\ d_{IPS}$ gives a very close value to the limit of the rule, and it can be safely used without the risk of buckling according to the calculations as well. However, the IPS with the smallest diameter ($0.57\ d_{IPS}$) may also endure the dynamic load without failure. This may be verified by buckling tests that are recommendations for future research.

VI. CONCLUSION

Buckling of interphase spacers during conductor vibration following ice shedding is studied in numerical and analytical models. The vibration following ice shedding is characterized by high amplitudes that are associated with excessive dynamic loads. Such high forces may lead to buckling of the spacer, which might cause permanent damage. The modern IPS consists of a special kind of composite made

of FRP that is characterized by high breaking strain. This makes the IPS withstand high compression loads that are greater than the Euler load for buckling, without plastic deformation. This means that such spacers can endure buckling without any permanent damage. Material tests are performed on different samples of that material to obtain its characteristics. In particular, the modulus of elasticity and the flexural strength were obtained from three-point bending tests.

Numerical simulations were conducted using the ANSYS software. The line-body model simulations consisted of two conductors and two IPSs, and it was used to obtain the displacements and the forces acting on the IPS during vibration following ice shedding from one of the conductors. Then, a more elaborated 3D model of the IPS was constructed to study the effects of dynamic loads on the spacer. Simulations were carried out for a typical case of ice accretion, i.e. ice thickness of 18 mm. Shedding of such accreted ice from the entire conductor in the set-up examined was followed by a peak axial load in the first cycle of conductor vibration. This load did not cause buckling in the IPS considered with a diameter of d_{IPS}, nor in the IPS whose diameter was $0.83d_{IPS}$ that would be closest to 1% of its length, which is preferable according to the rule of thumb for the selection of IPS. However, when the diameter was reduced to $0.57d_{IPS}$, then buckling occurred during the vibration following the modeled ice shedding phenomenon. The buckling angle was very small (less than 2°) even in this case, but the diameter is significantly smaller than 1% of its length. In order to obtain an accurate condition for the size of applicable IPS, additional buckling tests will be carried out.

A MATLAB application was developed as well to solve analytical equations in order to find the frequencies in different vibration modes, the tensile force, the sag of the loaded and the unloaded conductors, as well as to find the Euler load for buckling. This application can also calculate the largest possible Euler angle during the buckling of the IPS. The analytical and numerical models can help decide the most adequate choice for the IPS that does not suffer buckling in a specific configuration of the transmission line.

ACKNOWLEDGMENT

Project no. TKP2021-NVA-29 has been implemented with the support provided by the Ministry of Innovation and Technology of Hungary from the National Research, Development, and Innovation Fund, financed under the TKP2021-NVA funding scheme. Conference participation has been financed by the Mecenatúra MEC-R-21 funding scheme. The authors are grateful to the FCI Composite Insulator Ltd. for the active interest and providing the practical industrial experiences concerned.

REFERENCES

[1] "Pros and cons of underground power lines." Emergency Preparedness Partnerships. https://emergencypreparednesspartnerships.com/pros-and-cons-of-underground-power-lines/ (accessed March, 2022).

[2] P. Van Dyke, D. Havard, and A. Laneville, "Effect of Ice and Snow on the Dynamics of~ Transmission Line Conductors," in *Atmospheric Icing of Power Networks*: Springer, 2008, pp. 171-228.

[3] V.T. Morgan and D. A. Swift, "Jump height of overhead-line conductors after the sudden release of ice loads," *Central Electricity Research Laboratories, CEGB, Leatherhead, UK,* vol. 111, no. 10, pp. 1736 – 1746, 1964. [Online]. Available: https://digital-library.theiet.org/content/journals/10.1049/piee.1964.0285.

[4] A. Jamaleddine, G. McClure, J. Rousselet, and R. Beauchemin, "Simulation of ice-shedding on electrical transmission lines using ADINA," *Computers & structures,* vol. 47, no. 4-5, pp. 523-536, 1993. [Online]. Available: https://www.sciencedirect.com/science/article/pii/004579499390339F.

[5] L. E. Kollar and M. Farzaneh, "Modeling sudden ice shedding from conductor bundles," *IEEE Transactions on Power Delivery,* vol. 28, no. 2, pp. 604-611, 2013. [Online]. Available: https://ieeexplore.ieee.org/abstract/document/6387343.

[6] L. E. Kollár, M. Farzaneh, and P. Van Dyke, "Modeling ice shedding propagation on transmission lines with or without interphase spacers," *IEEE Transactions on Power Delivery,* vol. 28, no. 1, pp. 261-267, 2013. [Online]. Available: https://ieeexplore.ieee.org/abstract/document/6311448.

[7] B. Y. Chuan Wu, Liang Zhang, Bo Zhang, Qing Li, "A method to calculate jump height of iced transmission lines after ice-shedding," *Cold Regions Science and Technology,* pp. 40-47, 2016. [Online]. Available: https://doi.org/10.1016/j.coldregions.2016.02.001.

[8] G. Fu, L. Wang, Z. Guan, and X. Meng, "Study on the prevention of conductor ice-shedding by interphase spacer," in *2009 IEEE 9th International Conference on the Properties and Applications of Dielectric Materials*, 2009: IEEE, pp. 49-52.

[9] Y. Fujii and I. Suzuki, "Development of no-porcelain inter-phase spacer. Tadotai sodensen no shindo taisaku ni kansuru kenkyu. 1.; Hi jikisei sokan spacer no kaihatsu," *Soken Nenpo;(Japan),* vol. 23, 1991. [Online]. Available: https://www.osti.gov/etdeweb/biblio/5296956.

[10] R. C. Hibbeler, *Engineering mechanics 14th edition*. Pearson Prentice Hall Pearson Education, Inc. , 2016.

[11] H. M. Irvine and T. K. Caughey, "The linear theory of free vibrations of a suspended cable," *Proceedings of the Royal Society of London. A. Mathematical and Physical Sciences,* vol. 341, no. 1626, pp. 299-315, 1974. [Online]. Available: https://doi.org/10.1098/rspa.1974.0189.

[12] H. M. Irvine, "Cable structures," *MIT Press, Cambridge, MA,* 1981.

[13] K. J. Bathe, "Solution of Equilibrium Equations in Dynamic Analysis," in *Finite Element Procedures*, Second ed. United States of America: Prentice Hall, Pearson Education, Inc., 2014, ch. Nine, pp. 768-837.

[14] M. Roshan Fekr and G. McClure, "Numerical modelling of the dynamic response of ice-shedding on electrical transmission lines," *Atmospheric Research,* vol. 46, no. 1, pp. 1-11, 1998. [Online]. Available: https://doi.org/10.1016/S0169-8095(97)00046-X.

[15] L. Duan and W. Chen, "Effective length factors of compression members," *Structural engineering handbook,* 1999. [Online]. Available: https://scholar.google.com/scholar?hl=en&as_sdt=0%2C5&q=Effective+Length+Factors+of+Compression+Members&btnG=.

[16] S. P. Timoshenko and J. M. Gere, *Theory of elastic stability*. New York and London: Courier Corporation, 1961.